Asian Journal of Chemistry; Vol. 37, No. 11 (2025), 2745-2752
ASIAN JOURNAL OF CHEMISTRY
https://doi.org/10.14233/ajchem.2025.34429

Optimizing Metal Doping in *g*-C_3N_4: A Comprehensive Study of Palladium and Silver Nanocomposites for Enhanced Supercapacitor Performance

MONIKA DHANDA

Department of Chemistry, Deenbandhu Chhotu Ram University of Science and Technology, Murthal-131039, India

Corresponding author: E-mail: monikadhanda05@gmail.com

Received: 11 July 2025 *Accepted*: 20 September 2025 *Published online*: 27 October 2025 AJC-22162

This study extends previous work on Pd- and Ag-doped graphitic carbon nitride for advanced supercapacitor applications. Pure graphitic carbon nitride (*g*-C_3N_4, GCN) was synthesized *via* thermal polymerization, while metal doping was achieved by varying precursor concentrations. Comprehensive structural and morphological characterization was conducted using XRD, FT-IR and TEM. Enhanced electrochemical analyses cyclic voltammetry (CV), galvanostatic charge-discharge (GCD) and electrochemical impedance spectroscopy (EIS) were employed to assess charge transport and storage behaviour. Among all samples, PC9 (9 mmol Pd-doped GCN) exhibited the highest specific capacitance (401.1 F/g at 10 mV/s) and the lowest charge transfer resistance (R_{ct} = 1.10 Ω), indicating excellent redox activity and conductivity. In contrast, GCN–0.9Ag showed comparatively lower performance (195.3 F/g, R_{ct} = 19 Ω). The study confirms that optimal doping enhances electrochemical behaviour, while excess metal induces agglomeration and reduces efficiency. The optical properties of PC9 sample were also systematically investigated, reinforcing its potential as a multifunctional, high-performance electrode material for next-generation energy storage applications.

Keywords: Graphitic carbon nitride, Cyclic voltammetry, Galvanostatic charge-discharge, Specific capacitance.

INTRODUCTION

Electrochemical energy storage devices, particularly supercapacitors (SCs), have attracted considerable attention due to their high-power density, rapid charging and discharging rates, long cycle life and eco-friendly operation [1,2]. Unlike the traditional batteries, SCs offer faster kinetics and superior stability, making them ideal for applications in electric vehicles, hybrid transportation and portable electronics [3,4]. Despite their numerous advantages, the practical implementation of supercapacitors is frequently impeded by constraints in energy density and the performance of electrode materials. Consequently, the advancement of innovative electrode materials has become a primary area of research. Among the emerging candidates, graphitic carbon nitride (*g*-C_3N_4 or GCN) has attracted considerable attention [1,5]. GCN is a 2D, nitrogen rich polymeric material characterized by a layered structure similar to that of graphite [6,7]. It possesses favourable attributes such as high thermal and chemical stability, a tunable electronic structure, abundant nitrogen functional sites and straightforward, cost-effective synthesis from precursors like melamine or urea [8,9]. Its inherent π-conjugated system and lone pair electrons on nitrogen atoms enhance its electronic properties and electrochemical activity [10,11]. However, unmodified GCN typically experiences poor electrical conductivity and limited capacitance, which hinders its performance as a standalone electrode material. To mitigate these limitations, researchers have investigated metal doping strategies aimed at improving its surface area, conductivity and charge storage capacity [12,13].

To tackle these issues, researchers have examined the doping and hybridization of GCN with transition metals to boost its conductivity, surface redox activity and charge storage capability. Transition-metal-doped GCN systems, including Ni-, Co-, Fe- and Mn-based composites, have shown significant enhancements in performance. For $Ni(OH)_2$/Ni/*g*-C_3N_4 catalyst, a current density of 100 A cm^{-2} is attained at a relatively low overpotential of 1881 mV [14], accompanied by a minimal charge-transfer resistance of 10.86 Ω and a low Tafel slope of 44.3 mV dec^{-1}, indicating markedly superior electrocatalytic performance compared to pristine GCN. Similarly, CoS–Co_2O_3/*g*-C_3N_4 composites achieved 361 F g^{-1} in alkaline elec-

trolyte and an energy density of approximately 30 Wh kg^{-1} [15], while Cu–Fe_2O_3/*g*-C_3N_4 demonstrated 244 F g^{-1} retention after 2,000 cycles [16]. Despite these promising results, many first-row transition-metal-doped GCN composites still exhibit moderate conductivity and may suffer from structural instability during prolonged cycling.

In this research, pristine *g*-C_3N_4 (GCN) was synthesized through thermal polymerization and subsequently doped with specific amounts of Ag and Pd to develop a series of GCN–*x*Ag and GCN–*x*Pd composites. The integration of these noble metals into the GCN structure presents several significant benefits: (i) improved electrical conductivity, which facilitates quicker charge transfer and enhanced rate capability; (ii) consistent nanoparticle distribution, resulting in a higher number of electroactive sites and increased specific capacitance; and (iii) enhanced electrochemical and structural stability, leading to a prolonged cycle life. Moreover, both Pd and Ag are recognized for their ability to inhibit charge-carrier recombination, thus preserving capacitive performance even at elevated current densities. Notwithstanding these benefits, certain drawbacks must be recognized. The relatively high expense and limited natural availability of Pd and Ag pose challenges for large-scale, economically viable implementation. Furthermore, excessive loading of noble metals may lead to nanoparticle aggregation, which reduces the accessible surface area and adversely affects the electrochemical performance. Therefore, meticulous optimization of metal content, synthesis parameters and cost-effectiveness is crucial for the practical application of Pd/GCN and Ag/GCN composites in supercapacitor devices. Therefore, the main aim of this study was to systematically explore and compare the effects of Ag and Pd incorporation on the structural, morphological and electrochemical properties of GCN-based electrodes [17,18]. Extensive characterization techniques including cyclic voltammetry (CV), galvanostatic charge–discharge (GCD) and electrochemical impedance spectroscopy (EIS), were utilized to assess their electrochemical performance. The findings indicate that palladium and silver have distinct influences on capacitance behaviour, charge retention and cycling stability, offering valuable insights into the significance of noble-metal selection in enhancing the GCN-based materials for next-generation application.

EXPERIMENTAL

Synthesis: Table-1 summarizes the synthesis of pure and metal-doped *g*-C_3N_4 using a thermal polymerization method. Pure *g*-C_3N_4 is prepared by dissolving urea in water, drying it and calcinating at 550 ºC. For Pd- and Ag-doped variants, respective metal precursors ($PdCl_2$ or $AgNO_3$) were mixed with urea, followed by low-temperature drying and calcination under similar conditions. The doping levels are varied by changing the metal salt concentration [17-19]. All samples yield yellow powders indicating successful *g*-C_3N_4 formation with metal incorporation in Table-1.

Characterization: X-ray diffraction (XRD) analysis of all the synthesized samples was performed using a Rigaku Ultima IV diffractometer across a 2θ range of 10º–80º to investigate the crystalline structure and phase purity. FT-IR spectra were obtained using a Perkin-Elmer Frontier spectrometer within the 4000–400 cm^{-1} range, utilizing KBr pellets to detect functional groups and chemical bonding in the composites. Transmission electron microscopy (JEOL JEM-2100 Transmission Electron Microscope) was utilized to examine the morphology, particle size and structural arrangement of the synthesized materials, offering the comprehensive insights into their nanoscale characteristics.

RESULTS AND DISCUSSION

X-ray diffraction (XRD): The X-ray diffraction (XRD) patterns for $PdCl_2$, pristine *g*-C_3N_4 (GCN), PC9 and Ag-doped *g*-C_3N_4 (GCN-0.9Ag) are illustrated in Fig. 1. The diffraction peaks of $PdCl_2$ exhibit sharp and distinctly defined reflections, affirming its crystalline characteristics. Pristine GCN displays two prominent peaks at approximately 13.1º and 27.4º, which correspond to the (100) and (002) planes, respectively [1]. The (100) peak is attributed to the in-plane structural arrangement of tri-*s*-triazine units, while the pronounced (002) peak relates to the interlayer stacking of conjugated aromatic systems, aligning with the graphitic structure of *g*-C_3N_4 [2]. In case of the PC9 composite, the diffraction pattern reveals a slight shift and broadening of the (002) peak in comparison to pristine GCN, indicating partial structural alteration and improved dispersion resulting from composite formation [18]. The GCN-0.9Ag sample also exhibits a similar pattern, with a further reduction in peak intensity and broadening, suggesting effective Ag doping, which leads to slight lattice distortion and a decrease in crystallite size [17]. The lack of distinct Ag-related peaks can be explained by the high dispersion of Ag nanoparticles within the *g*-C_3N_4 matrix or their diminutive size, which may be below the detection threshold of XRD. In summary, the XRD analysis validates the structural integrity of *g*-C_3N_4 post-doping and emphasizes the successful incorporation of Ag without compromising the fundamental layered structure.

TABLE-1
COMPARATIVE SYNTHESIS ROUTES FOR PURE, Pd-DOPED AND Ag-DOPED *g*-C_3N_4 COMPOSITES

Sample	Precursors used	Preparation conditions	Calcination conditions	Final product description
GCN (pure)	10 g Urea + 20 mL distilled water	Urea dissolved, stirred 30 min → Dried in hot air oven	550 ºC for 5 h (ramp rate: 2 ºC/min) in muffle furnace	Yellow powder of *g*-C_3N_4
Pd-doped GCN (PC)	10 g Urea + x mmol $PdCl_2$ + 20 mL distilled water	$PdCl_2$ and urea solutions mixed and stirred at 40 ºC until clear → Dried at 80 ºC for 2 h	550 ºC for 4 h (ramp rate: 2 ºC/min)	Yellow Pd-doped GCN powders (PC3, PC6, PC9, PC12)
Ag-doped GCN	10 g Urea + x mmol $AgNO_3$ + 20 mL distilled water	$AgNO_3$ and urea solutions mixed and stirred at 40 ºC until clear → Dried at 90 ºC for 3 h	550 ºC for 4 h (ramp rate: 2 ºC/min)	Yellow Ag-doped GCN powders (GCN–0.3Ag to GCN–3Ag)

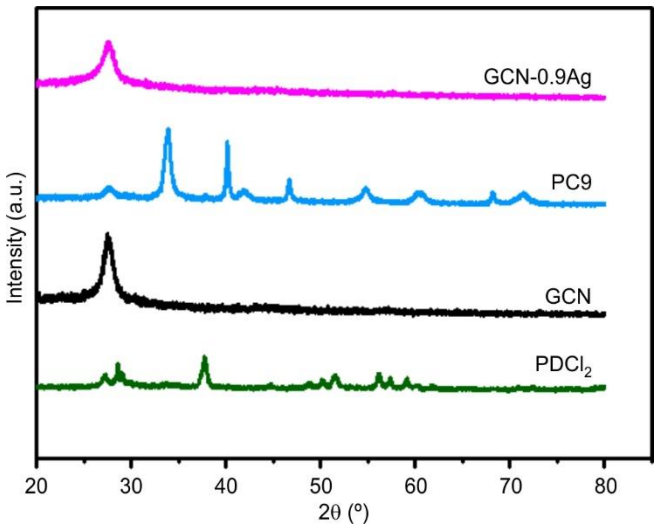

Fig. 1. XRD spectra of $PdCl_2$, GCN, PC9 and GCN-0.9Ag

FT-IR spectral studies: The FT-IR spectra for pristine g-C_3N_4 (GCN), Ag-doped g-C_3N_4 (GCN-0.9Ag) and the Pd-doped g-C_3N_4 PC9 composite are shown in Fig. 2. The pristine GCN displays several distinctive vibrational bands within the range of 1650-1200 cm^{-1}, which can be linked to the stretching modes of C–N and C=N heterocycles, thereby confirming the existence of tri-*s*-triazine units that constitute the g-C_3N_4 framework [1]. A prominent peak located around 810 cm^{-1} is associated with the breathing mode of the tri-*s*-triazine ring, serving as a characteristic feature of g-C_3N_4 [2]. Furthermore, the broad absorption band observed in the 3500-3000 cm^{-1} range is related to the stretching vibrations of N–H/O–H groups, likely resulting from adsorbed moisture or terminal amino groups. For GCN-0.9Ag, the overall spectral profile remains largely unchanged, indicating that the fundamental heptazine structure of g-C_3N_4 is maintained following Ag doping. Nevertheless, minor shifts and variations in peak intensity are observed, suggesting a successful interaction between Ag and the g-C_3N_4 network, which leads to subtle alterations in the local chemical environment [17]. The PC9 composite reveals the additional features and enhanced bands, which can be attributed to synergistic interactions among the components within the composite, further validating the successful formation of PC9 [18]. These spectral modifications reinforce the effective incorporation of dopants or composite constituents while preserving the primary structural integrity of g-C_3N_4.

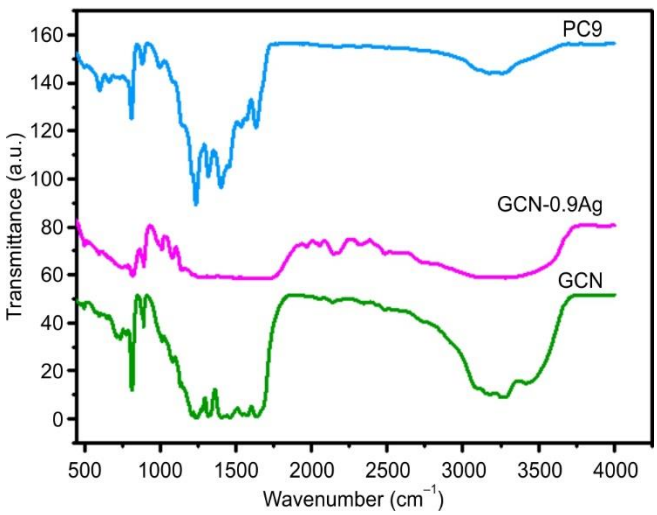

Fig. 2. FT-IR spectra of GCN, GCN-0.9Ag and PC9

Thermal studies: The thermogravimetric analysis (TGA) curves for pristine GCN, Ag-doped GCN (GCN-0.9Ag) and PC9 are shown in Fig. 3 to assess their thermal stability. Pristine GCN demonstrates excellent thermal stability up to approximately 500 ºC, with significant weight loss occurring between 500-750 ºC, which is attributed to the thermal decomposition of the heptazine units and the eventual degradation of the g-C_3N_4 framework [2]. GCN-0.9Ag exhibits a similar decomposition profile but with slightly reduced weight loss, indicating that the incorporation of Ag enhances thermal stability by reinforcing the g-C_3N_4 network [17]. Conversely, the PC9 composite shows an earlier onset of weight loss, commencing around 450 ºC, which may be due to the presence of Pd in the GCN that decomposes at relatively lower temperatures. Nonetheless, PC9 retains a considerable amount of residue even after reaching 750 ºC, suggesting the existence of thermally stable species that remain undecomposed [18]. In summary, the TGA results affirm that all samples exhibit good thermal stability, with GCN-0.9Ag and PC9 showing slightly enhanced resistance to thermal degradation, which is advantageous for high-temperature electrochemical applications.

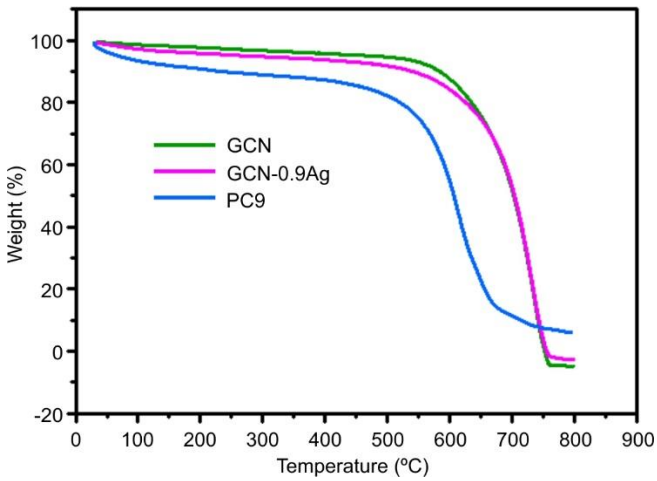

Fig. 3. TGA curves of GCN, GCN-0.9Ag and PC9

Transmission electron microscopy (TEM): The TEM image of GCN-0.9Ag (Fig. 4a) reveals a relatively compact, layered sheet-like structure characterized by slight wrinkling, which is typical of thermally polymerized g-C_3N_4 [1]. The uniform contrast suggests a consistent dispersion of Ag species throughout the g-C_3N_4 framework, indicating successful doping without significant agglomeration [17]. In contrast, the TEM image of PC9 (Fig. 4b) shows a more exfoliated and loosely stacked nanosheet morphology. The presence of thin layers and interconnected porous networks is distinctly observable, which indicates that Pd incorporation disrupts the regular stacking of g-C_3N_4 layers and promotes exfoliation. This structural alteration is advantageous for electrochemical applications, as it increases the accessible surface area and enhances electrolyte penetration, thereby facilitating efficient ion transport. These findings confirm that both Ag and Pd doping maintain

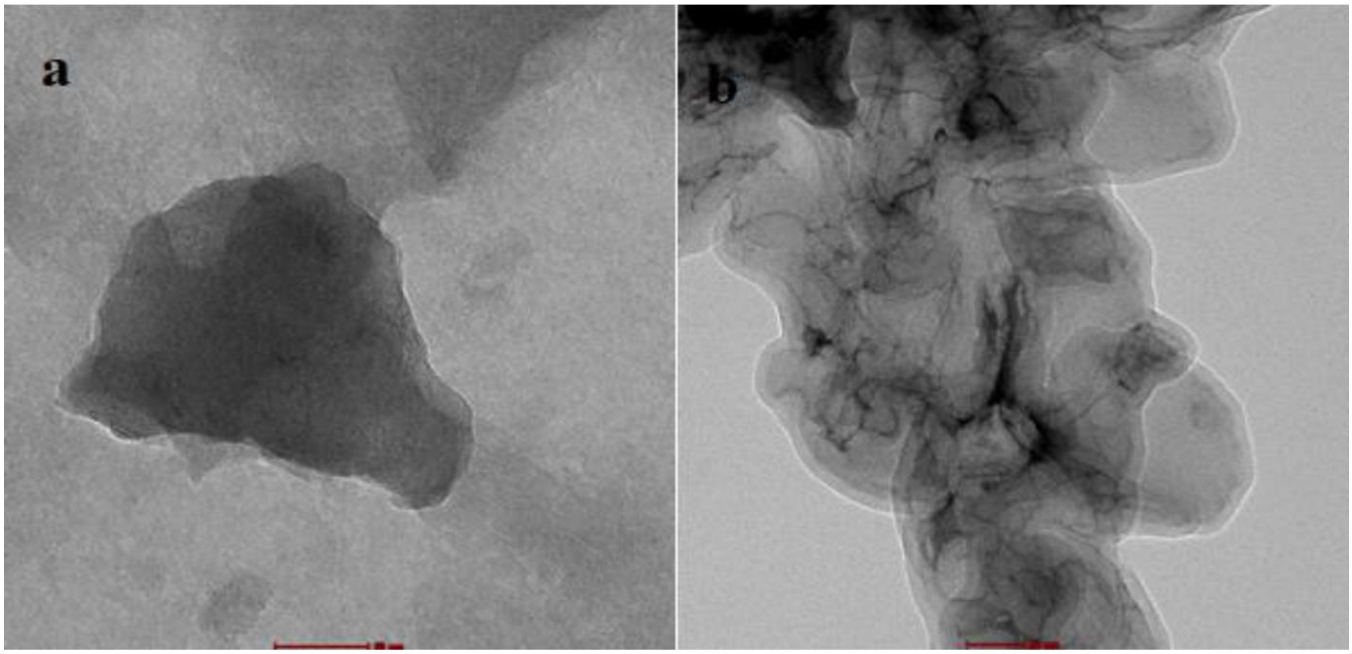

Fig. 4. TEM images of (a) GCN-0.9Ag and (b) PC9

the fundamental layered structure of *g*-C_3N_4 while inducing nanoscale modifications that are beneficial for supercapacitor performance.

Electrochemical performance: To investigate the electrochemical performance of *g*-C_3N_4, polypyrrole (PPy) and their composites, measurements were carried out using a PGSTAT 204 Autolab electrochemical workstation (Metrohm, Netherlands) equipped with the FRA32M module and controlled *via* Nova software. A conventional three-electrode setup and two electrode setups as employed for all electrochemical tests [1]. In this configuration, the working electrode consisted of the substrate coated with the active material [17-20]. A platinum wire served as the counter electrode and an Ag/AgCl electrode was used as the reference electrode.

Cyclic voltammetry (CV), galvanostatic charge–discharge (GCD) and electrochemical impedance spectroscopy (EIS) were performed to evaluate the electrochemical behaviour and working potential of the electrode materials [20-24]. Specifically, the specific capacitance of the synthesized composites was determined using both CV and GCD techniques [1]. The specific capacitance (Cv) from CV was calculated using eqn. 1:

$$Cv = \int \frac{IdV}{\nu m \Delta V} \quad (1)$$

where Cv = specific capacitance measured from CV curves in F/g, I = current in A; ΔV = applied potential window in V; m = mass of the sample loaded on the surface of the electrode in mg; and ν = scan rate in mV/s.

Similarly, the specific capacitance (Cs) from GCD curves was determined using eqn. 2:

$$Cs = \frac{I\Delta t}{m\Delta V} \quad (2)$$

where Cs = specific capacitance which is measured from GCD in F/g, I = applied current in A; m = deposited mass on electrode in mg; ΔV = applied potential window in V; Δt = time of discharge in s.

The energy density and power density were further calculated to assess the practical performance of the materials using eqns. 3 and 4 [17]:

$$E = \left(\frac{1}{2 \times 3.6}\right)(C \times \Delta V^2) \quad (3)$$

where E = energy density in W h/Kg; C = specific capacitance in F/g; ΔV = applied potential window in V.

$$P = 3600 \times \left(\frac{E}{t}\right) \quad (4)$$

where P = power density in W/Kg and t = discharge time in s from GCD.

A comparative assessment of the electrochemical properties of Pd-doped and Ag-doped *g*-C_3N_4 composites is presented in Table-2, focusing on the specific capacitance and areal capacitance at a scan rate of 10 mV/s.

Cyclic voltammetry (CV): The data obtained from cyclic voltammetry (CV) offer a thorough insight into the specific capacitance (SC) characteristics of Pd-doped and Ag-doped *g*-C_3N_4 composites under different current densities. Among the samples examined, PC9, which contains 9 mmol of Pd, consistently exhibits the highest specific capacitance value of 401.1 F/g, especially at lower current densities. This remarkable performance is attributed to the optimized distribution of Pd nanoparticles within the *g*-C_3N_4 matrix, which improves both electronic conductivity and the electrochemical surface area. In contrast, GCN–0.9Ag, which is doped with 0.9 mmol of silver, reaches a maximum specific capacitance of 195.3 F/g (Fig. 5), significantly lower than that of PC9, yet still showing a significant enhancement compared to undoped *g*-C_3N_4 (Table-3). This comparative analysis reveals two significant trends. First, both Pd- and Ag-doped composites demonstrate an initial rise in capacitance as the metal concentration increases, peaking at optimal doping levels (9 mmol for Pd and 0.9 mmol for Ag). Beyond these optimal concentrations, a decrease

TABLE-2
COMPARATIVE SPECIFIC AND AREAL CAPACITANCE DATA OF Pd- AND Ag-DOPED g-C_3N_4 AT 10 mV/s

Sample	Pd/Ag content	Mass loading (mg/cm^2)	Specific capacitance (F/g)	Areal capacitance (F/cm^2)
GCN	–	–	16.3	0.03
PC3	3 mmol Pd	–	39.5	0.18
PC6	6 mmol Pd	–	171.2	0.27
PC9	9 mmol Pd	–	401.1	0.41
PC12	12 mmol Pd	–	174.4	0.31
GCN–P	0 mmol Ag	1.24	21.2	–
GCN–0.3Ag	0.3 mmol Ag	1.28	32.6	–
GCN–0.6Ag	0.6 mmol Ag	1.30	138.4	–
GCN–0.9Ag	0.9 mmol Ag	1.60	195.3	–
GCN–1.2Ag	1.2 mmol Ag	1.33	85.5	–
GCN–2.0Ag	2.0 mmol Ag	1.21	21.7	–
GCN–3.0Ag	3.0 mmol Ag	1.51	7.1	–

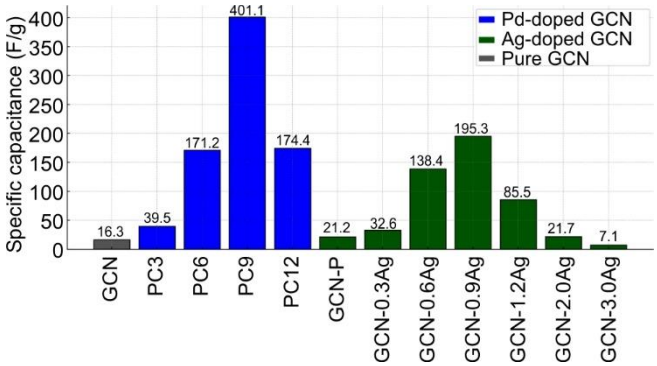

Fig. 5. Bar representation of specific capacitance of Pd and Ag doped g-C_3N_4 at 10 mV/s

TABLE-3
COMPARISON DATA OF SPECIFIC AND AREAL CAPACITANCE OF PC9 AND GCN–0.9Ag AT DIFFERENT SCAN RATES [Ref. 17,18,25]

Scan rate (mV/s)	Specific capacitance of PC9 (F/g)	Areal capacitance of PC9 (F/cm^2)	Specific capacitance of GCN–0.9Ag (F/g)
10	401.1	0.61	195.3
20	238.2	0.41	117.1
30	188.2	0.32	104.1
40	161.7	0.28	–
50	141.1	0.24	95.0
60	127.4	0.22	–
70	117.6	0.20	–
80	110.2	0.18	–
90	100.6	0.17	–
100	94.2	0.16	–

in performance is observed, primarily due to the agglomeration of metal particles and the saturation of active surface sites, which impede ion transport and effective charge storage. Secondly, the Pd-doped composites demonstrate consistently higher performance than the Ag-doped counterparts at all current densities, attributable to improved charge transfer kinetics, enhanced conductivity and more abundant redox-active surface sites introduced by palladium.

Galvanostatic charge-discharge (GCD): The galvanostatic charge-discharge (GCD) analysis of Pd- and Ag-doped g-C_3N_4 composites provides valuable insights into their electrochemical characteristics, especially regarding reversibility, capacitance and energy–power dynamics. In case of the Pd-doped series (PC3–PC12), the specific capacitance (SP) increases with higher Pd content up to 9 mmol (PC9), which is attributed to the greater number of redox-active sites and improved electronic conductivity. However, when the doping level is raised to 12 mmol (PC12), a decrease in SP is observed, likely due to the agglomeration or oversaturation of active sites that impede effective charge storage. Among the Pd-doped samples, PC9 stands out with the highest specific capacitance of 328.8 F/g at 1.0 A/g, marking it as the most favourable formulation. As the current density rises, a typical reduction in discharge time is observed, resulting from diffusion limitations and a narrowed charge storage window. Nevertheless, PC9 retains a relatively higher capacitance even at increased current densities, indicating excellent rate capability and electrode stability. Conversely, the Ag-doped series (GCN–Ag) achieves its optimal performance with 0.9 mmol Ag loading (GCN–0.9Ag), reaching a specific capacitance of 207.0 F/g at 0.5 A/g (Table-4). As the Ag concentration escalates to 1.2 mmol, a significant drop in capacitance is observed, potentially due to excessive Ag blocking active surface sites and reducing electrochemical activity. While GCN–0.9Ag shows stable performance across different current densities, its specific capacitance also declines at higher current rates due to kinetic and diffusion limitations. A comparative evaluation of energy and power densities at varying current densities further emphasizes the differing behaviours of these two composites. For PC9, at a current density of 1.0 A g^{-1}, the energy density shows a remarkable increase, reaching 50.3 Wh kg^{-1}, while the power density drops to 45.7 W kg^{-1}. This behaviour suggests that PC9 is particularly suited for applications prioritizing high energy storage over longer discharge periods. In contrast, GCN–0.9Ag demonstrates the opposite trend: its energy density decreases from 10.35 Wh kg^{-1} at 0.5 A g^{-1} to 8.35 Wh kg^{-1} at 1.0 A g^{-1}, whereas its power density rises significantly from 135.9 W kg^{-1} to 272.0 W kg^{-1}, indicating its suitability for applications demanding rapid power delivery.

Electrochemical impedance spectroscopy (EIS): To highlight differences in electrochemical behaviour, Table-5 summarizes the fitted electrochemical impedance spectroscopy (EIS) parameters like R_s, R_{ct}, CPE, n, C_{dl} and electron transfer resistance for Pd-doped and Ag-doped composites, corresponding to the Nyquist plots shown in Fig. 6 [28,29].

TABLE-4
GCD-DERIVED SPECIFIC CAPACITANCE (SP) DATA OF Pd- AND Ag-DOPED *g*-C_3N_4 COMPOSITES AT DIFFERENT CURRENT DENSITIES [Ref. 17,18,26,27]

Sample	Dopant conc.	Current density (A/g)	Specific capacitance (F/g)	Conclusion
GCN	–	1.0	11.1	Baseline value for undoped GCN
PC3	3 mmol Pd	1.0	53.2	Moderate increase in SP with Pd doping
PC6	6 mmol Pd	1.0	140.1	Significant improvement in SP
PC9	9 mmol Pd	1.0	328.8	Maximum SP achieved among Pd-doped series
PC12	12 mmol Pd	1.0	313.3	Slight decrease in SP, suggesting saturation beyond 9 mmol Pd
PC9	9 mmol Pd	1.5	–	GCD curve provided, but SP value not mentioned
PC9	9 mmol Pd	2.0	–	
PC9	9 mmol Pd	2.5	–	
PC9	9 mmol Pd	3.0	–	Shows decreasing trend in discharge time with increasing current density
GCN–0.6Ag	0.6 mmol Ag	0.5	144.9	Gradual increase with doping
GCN–0.9Ag	0.9 mmol Ag	0.5	207.0	Peak SP among Ag-doped samples
GCN–1.2Ag	1.2 mmol Ag	0.5	70.66	Decline in SP, indicating over-doping
GCN–0.9Ag	0.9 mmol Ag	1.0	167.0	SP decreases slightly as current density increases
GCN–0.9Ag	0.9 mmol Ag	1.5	165.4	Nearly stable compared to 1.0 A/g
GCN–0.9Ag	0.9 mmol Ag	2.0	60.5	Sharp decline due to diffusion limitations

TABLE-5
COMPARATIVE EIS DATA OF Pd- AND Ag-DOPED *g*-C_3N_4 COMPOSITES

Sample	Dopant	R_s (Ω)	R_{ct} (Ω)	CPE (mMHO)	n	C_{dl} (mF)	Conclusion
PC3	3 mmol Pd	8.42	54.9	6.09	0.67	0.885	Moderate resistance; initial improvement in conductivity
PC6	6 mmol Pd	8.45	67.4	6.14	0.66	0.876	Slight increase in R_{ct}; optimal doping not yet reached
PC9	9 mmol Pd	2.74	1.10	5.97	0.85	1.12	Lowest R_{ct} and highest C_{dl}; best electrochemical performance
PC12	12 mmol Pd	8.50	1.23	6.42	0.65	0.786	R_{ct} slightly increased; possible agglomeration at higher Pd content
GCN–P	Pure GCN	–	198	–	–	–	Highest R_{ct} among all; limited charge transfer
GCN–0.6Ag	0.6 mmol Ag	–	90	–	–	–	Noticeable reduction in R_{ct} due to Ag doping
GCN–0.9Ag	0.9 mmol Ag	–	19	–	–	–	Lowest R_{ct} among Ag composites; best charge transfer
GCN–1.2Ag	1.2 mmol Ag	–	71	–	–	–	Increase in R_{ct} after optimum 0.9 mmol Ag; indicates dopant saturation effect

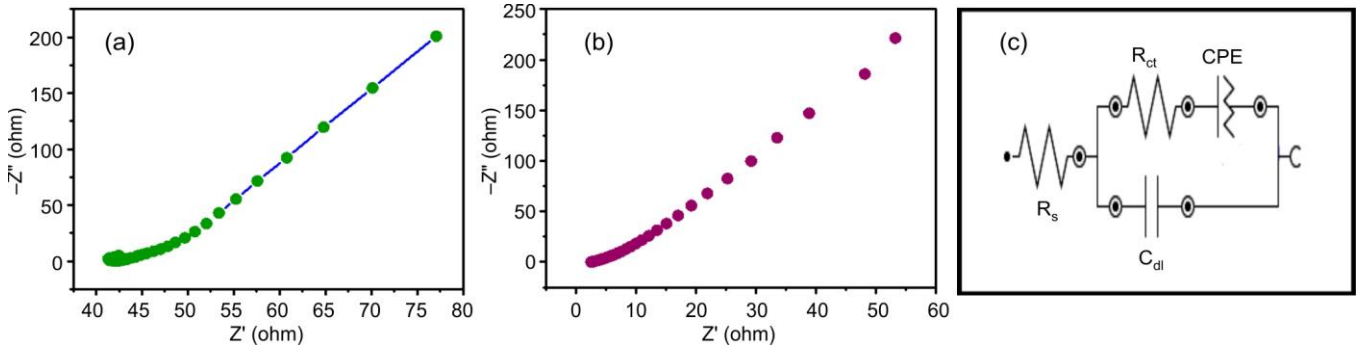

Fig. 6. (a) Nyquist plots of GCN-0.9Ag, (b) PC9, and (c) electrical equivalent circuit

Cyclic stability: The cyclic stability profiles of GCN-0.9Ag (Fig. 7a) and PC9 (Fig. 7b) illustrate the long-term durability of the electrodes over 10,000 continuous cycles [30-32]. GCN-0.9Ag shows an initial capacitance retention close to 100%, followed by a gradual decrease, ultimately maintaining 91.6% retention after 10,000 cycles. This suggests moderate structural stability, with some loss of active sites or slight agglomeration occurring during extended cycling. In contrast, PC9 (9 mmol Pd-doped GCN) demonstrates superior cycling stability, retaining approximately 93.9% of its initial capacitance at the conclusion of 10,000 cycles, with less fluctuation throughout the testing period. This enhanced stability can be attributed to the strong interaction between Pd nanoparticles and the *g*-C_3N_4 matrix, which improves charge transfer kinetics and mitigates significant electrode degradation. In summary, the data confirm that Pd doping not only enhances specific capacitance, but also significantly boosts the long-term electrochemical durability of *g*-C_3N_4-based electrodes, positioning PC9 as a more dependable candidate for practical supercapacitor applications. Table-6 represents the electrochemical performance of *g*-C_3N_4-based electrode materials.

Conclusion

In this comprehensive study, Pd- and Ag-doped *g*-C_3N_4 nanocomposites were systematically synthesized and evaluated to determine the most effective electrode material for super-

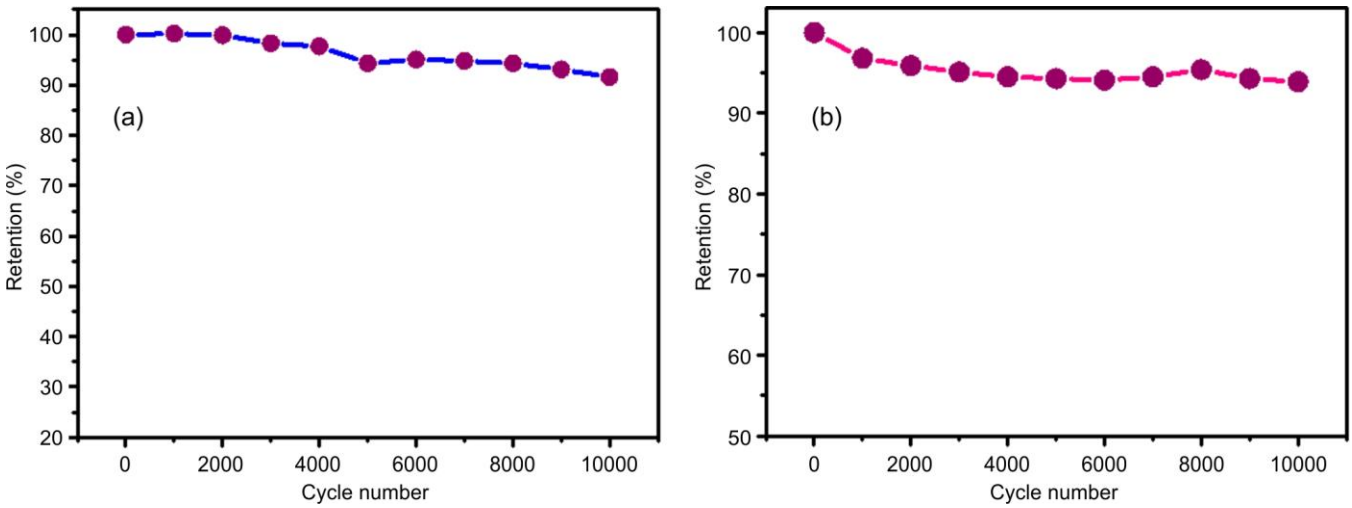

Fig. 7. (a) Cyclic stability of GCN-0.9Ag and (b) cyclic stability of PC9

TABLE-6
COMPARATIVE ELECTROCHEMICAL PERFORMANCE DATA OF g-C_3N_4 BASED ELECTRODE MATERIALS

Electrode material	Electrolyte	Scan rate	Specific capacitance (F/g)	Cycle retention	Ref.
ppy/g-C_3N_4	6 M KOH	–	471.0	71% (after 5000 cycles)	[32]
V_2O_5/g-C_3N_4	1 M H_2SO_4	–	457.0	84% (after 1000 cycles)	[33]
$FeWO_4$ nanorods/g-C_3N_4	–	–	357.0	80% (after 1000 cycles)	[34]
CoAl layered double hydroxide/g-C_3N_4	2.0 M KOH	5.0 A/g	343.3	93% (after 6000 cycles)	[35]
MnO_2/Polypyrrole/g-C_3N_4	0.5 M Na_2SO_4	2.0 A/g	274.0	95% (after 1000 cycles)	[36]
PEDOT: PSS/g-C_3N_4	1 M H_2SO_4	–	137.0	89% (after 1000 cycles)	[37]
TiO_2/g-C_3N_4	2.0 M KOH	1.0 A/g	125.1	100% (after 1000 cycles)	[38]
Polyindole/g-C_3N_4	1 M H_2SO_4	2.0 A/g	115.8	96% (after 250 cycles)	[39]
$ZnFe_2O_4$/g-C_3N_4	6 M KOH	10 mV/s	103.0	94% (after 500 cycles)	[40]
Gold/g-C_3N_4	0.5 M Na_2SO_4	–	98.0	100% (after 1000 cycles)	[41]
AgNPs@g-C_3N_4	1 M Na_2SO_4	1.0 A/g	28.8	78.9% (after 1000 cycles)	[42]

capacitor applications. This research included thorough electrochemical assessments such as CV, GCD and EIS, along with additional performance metrics and structural analyses. The comparative results indicated that metal doping significantly improves the electrochemical performance of g-C_3N_4 by enhancing its conductivity, redox activity and surface charge storage. Among all the samples tested, 9 mmol Pd-doped composite (PC9) consistently outperformed the others, demonstrating the highest specific capacitance (401.1 F/g at 10 mV/s), superior areal capacitance and the lowest charge transfer resistance (1.10 Ω). These enhancements are attributed to the strong interaction between Pd and nitrogen sites within the g-C_3N_4 matrix, facilitating effective charge transport and increasing the electroactive surface area. While Ag doping also resulted in visible improvements, its optimal performance (195.3 F/g for GCN–0.9Ag) was comparatively lower and higher concentrations led to performance degradation due to potential agglomeration and site saturation. This research not only validates the effectiveness of Pd as a dopant in modifying the electrochemical properties of g-C_3N_4 but also emphasizes the significance of precise dopant control. Moreover, it provides a comprehensive understanding of the structure-property relationships in these composites. Overall, the PC9 sample stands out as the most promising candidate for future high-performance supercapacitor systems and potentially for multifunctional energy storage technologies.

ACKNOWLEDGEMENTS

The author gratefully acknowledges the Department of Chemistry, Deenbandhu Chhotu Ram University of Science and Technology, Murthal, India for providing the necessary research facilities and instrumental support throughout the course of this study.

CONFLICT OF INTEREST

The authors declare that there is no conflict of interests regarding the publication of this article.

REFERENCES

1. M. Dhanda, R. Arora, M. Saini, S.P. Nehra and S. Lata, *New J. Chem.*, **46**, 14215 (2022); https://doi.org/10.1039/D2NJ02401B
2. M. Dhanda, S.P. Nehra and S. Lata, *Synth. Met.*, **286**, 117046 (2022); https://doi.org/10.1016/j.synthmet.2022.117046
3. Z. Lin, E. Goikolea, A. Balducci, K. Naoi, P.L. Taberna, M. Salanne, G. Yushin and P. Simon, *Mater. Today*, **21**, 419 (2018); https://doi.org/10.1016/j.mattod.2018.01.035
4. Q. Xue, J. Sun, Y. Huang, M. Zhu, Z. Pei, H. Li, Y. Wang, N. Li, H. Zhang, and C. Zhi, *Small*, **13**, 1701877 (2017); https://doi.org/10.1002/smll.201701827
5. J. Kowal, E. Avaroglu, F. Chamekh, A. Šenfelds, T. Thien, D. Wijaya and D.U. Sauer, *J. Power Sources*, **196**, 573 (2011); https://doi.org/10.1016/j.jpowsour.2009.12.028

6. M. Yadav, M. Dhanda, R. Arora, R. Jagdish, G. Singh and S. Lata, *New J. Chem.*, **46**, 12783 (2022); https://doi.org/10.1039/D2NJ01892F
7. M. Yadav, G. Singh and S. Lata, *J. Solid State Electrochem.*, **26**, 2153 (2022); https://doi.org/10.1007/s10008-022-05216-9
8. Meenu, P. Kumar and B.S. Dehiya, *J. Nanosci. Technol.*, **5**, 584 (2019); https://doi.org/10.30799/jnst.195.19050102
9. M. Dhanda, R. Arora, S. Ahlawat, S.P. Nehra and S. Lata, *J. Energy Storage*, **52**, 104740 (2022); https://doi.org/10.1016/j.est.2022.104740
10. S. Lee, I.N. Ivanov, J.K. Keum and H.N. Lee, *Sci. Rep.*, **6**, 19621 (2016); https://doi.org/10.1038/srep19621
11. R.B. Rakhi, D.H. Nagaraju, P. Beaujuge and H.N. Alshareef, *Electrochim. Acta*, **220**, 601 (2016); https://doi.org/10.1016/j.electacta.2016.10.109
12. Y. Zheng, J. Liu, J. Liang, M. Jaroniec and S. Z. Qiao, *Energy Environ. Sci.*, **5**, 6717 (2012); https://doi.org/10.1039/C2EE03479D
13. Z. Han, N. Wang, H. Fan and S. Ai, *Solid State Sci.*, **65**, 110 (2017); https://doi.org/10.1016/j.solidstatesciences.2017.01.010
14. J. Zhang, Y. Zhao, A.-L. Wu, J. Li and Y.-X. Wang, *J. Fuel Chem. Technol.*, **4**, 198 (2021); https://doi.org/10.1016/S1872-5813(21)60010-5
15. M. Rabia, D. Essam, F.H. Alkallas, M. Shaban, S. Elaissi and A.B.G. Trabelsi, *Micromachines*, **13**, 2234 (2022); https://doi.org/10.3390/mi13122234
16. C. Harak, V. Kadam, R. Gavhane, S. Balgude, A. Rakshe, S. Uke, N. Brahmankar, D. Satpute, H. Pawar and S. Mardikar, *RSC Adv.*, **14**, 4917 (2024); https://doi.org/10.1039/d3ra08428k
17. M. Dhanda, S.P. Nehra and S. Lata, *Russ. J. Electrochem.*, **59**, 248 (2023); https://doi.org/10.1134/S1023193523030047
18. M. Dhanda, R. Arora, M. Yadav, S. Ahlawat, S. Dahiya, D.R. Paul, G. Jha, G. Singh, S.P. Nehra and S. Lata, *Mater. Sci. Eng. B*, **304**, 117344 (2024); https://doi.org/10.1016/j.mseb.2024.117344
19. J. Zhang, L. Chen, Y. Wang, S. Cai, H. Yang, H. Yu, F. Ding, C. Huang and X. Liu, *Nanomaterials*, **8**, 1020 (2018); https://doi.org/10.3390/nano8121020
20. E. Amichai and N. Kronfeld-Schor, *Sci. Rep.*, **9**, 11052 (2019); https://doi.org/10.1038/s41598-019-47544-3
21. S. Yao, S. Xue, S. Peng, M. Jing, X. Qian, X. Shen, T. Li and Y. Wang, *J. Mater. Sci. Mater. Electron.*, **29**, 17921 (2018); https://doi.org/10.1007/s10854-018-9906-2
22. K. Katsumata, R. Motoyoshi, N. Matsushita and K. Okada, *J. Hazard. Mater.*, **260**, 475 (2013); https://doi.org/10.1016/j.jhazmat.2013.05.058
23. A. Kharlamov, M. Bondarenko, G. Kharlamova and N. Gubareni, *Diamond Rel. Mater.*, **66**, 16 (2016); https://doi.org/10.1016/j.diamond.2016.03.012
24. G. Ren, R. Zhang and Z. Fan, *Appl. Surf. Sci.*, **441**, 466 (2018); https://doi.org/10.1016/j.apsusc.2018.02.059
25. R. Basu, S. Ghosh, S. Bera, A. Das and S. Dhara, *Sci. Rep.*, **9**, 40225 (2019); https://doi.org/10.1038/s41598-019-40225-1
26. C. Zhong, Y. Deng, W. Hu, J. Qiao, L. Zhang and J. Zhang, *Chem. Soc. Rev.*, **44**, 7484 (2015); https://doi.org/10.1039/C5CS00303B
27. J. Ma, X.-Y. Tao, S.-X. Zhou, X.-Z. Song, Lin-Guo, Yao-Wang, Y.-B. Zhu, L.-T. Guo, Z.-S. Liu, H.-L. Fan and X.-Y. Wei, *J. Electroanal. Chem.*, **835**, 346 (2019); https://doi.org/10.1016/j.jelechem.2018.12.025
28. R. Arora, M. Dhanda, M. Yadav, R. Malik, P. Pahuja, S. Ahlawat, V.S. Rao, S.P. Nehra and S. Lata, *Solid State Ion.*, **403**, 116402 (2023); https://doi.org/10.1016/j.ssi.2023.116402
29. M. Dhanda, R. Arora, M. Yadav, P. Pahuja, S. Ahlawat, S.P. Nehra and S. Lata, *Mater. Sci. Eng. B*, **300**, 117055 (2024); https://doi.org/10.1016/j.mseb.2023.117055
30. M. Yadav, M. Dhanda, R. Arora, S. Ahlawat, G. Singh, K. Nehra, and S. Lata, *Mater. Sci. Eng. B*, **297**, 116719 (2023); https://doi.org/10.1016/j.mseb.2023.116719
31. M. Manisha, M. Dhanda, R. Arora, A.S. Reddy, S. Lata and A. Sharma, *J. Alloys Compd.*, **955**, 169738 (2023); https://doi.org/10.1016/j.jallcom.2023.169738
32. G. Dong, H. Fan, K. Fu, L. Ma, S. Zhang, M. Zhang, J. Ma and W. Wang, *Compos., Part B Eng.*, **162**, 369 (2019); https://doi.org/10.1016/j.compositesb.2018.12.098
33. Y. Zhou, L. Sun, D. Wu, X. Li, J. Li, P. Huo, H. Wang and Y. Yan, *J. Alloys Compd.*, **817**, 152707 (2020); https://doi.org/10.1016/j.jallcom.2019.152707
34. D.P. Ojha, H.P. Karki, J. Song and H.J. Kim, *Chem. Phys. Lett.*, **712**, 83 (2018); https://doi.org/10.1016/j.cplett.2018.09.070
35. S. Sanati and Z. Rezvani, *Chem. Eng. J.*, **362**, 743 (2019); https://doi.org/10.1016/j.cej.2019.01.081.
36. S. Sun, L. Guo, X. Chang, Y. Yu and X. Zhai, *Mater. Lett.*, **236**, 558 (2019); https://doi.org/10.1016/j.matlet.2018.11.001
37. X. Chen, X. Zhu, Y. Xiao and X. Yang, *J. Electroanal. Chem.*, **743**, 99 (2015); https://doi.org/10.1016/j.jelechem.2015.02.004
38. Y. Zhao, L. Xu, S. Huang, J. Bao, J. Qiu, J. Lian, L. Xu, Y. Huang, Y. Xu and H. Li, *J. Alloys Compd.*, **702**, 178 (2017); https://doi.org/10.1016/j.jallcom.2017.01.125
39. C.J. Verma, A.S. Keshari, P. Dubey and R. Prakash, *Vacuum*, **177**, 109363 (2020); https://doi.org/10.1016/j.vacuum.2020.109363
40. B. Palanivel, S. Mudisoodum perumal, T. Maiyalagan, V. Jayarman, C. Ayyappan and M. Alagiri, *Appl. Surf. Sci.*, **498**, 143807 (2019); https://doi.org/10.1016/j.apsusc.2019.143807
41. A.Y. Chen, T.T. Zhang, Y.J. Qiu, D. Wang, P. Wang, H.J. Li, Y. Li, J.H. Yang, X.Y. Wang and X.F. Xie, *Electrochim. Acta*, **294**, 260 (2019); https://doi.org/10.1016/j.electacta.2018.10.106
42. D.F. Wang, Y.Z. Wu, X.H. Yan, J.J. Wang, Q. Wang, C. Zhou, X.X. Yuan, J.M. Pan and X.N. Cheng, *MRS Commun.*, **9**, 719 (2019); https://doi.org/10.1557/mrc.2019.25